Journal of Earth Science, *Vol. 36*, *No. 4*, *p. 1632-1649*, *August 2025* *ISSN 1674-487X*
Printed in China
https://doi.org/10.1007/s12583-023-1833-3

New Understandings of the Shaziba Landslide-Debris Flow in Hubei Province, China

Taiyi Chen[1], **Guangli Xu**[*1], **Tetsuya Hiraishi**[2]
1. *Faculty of Engineering*, *China University of Geosciences* (*Wuhan*), *Wuhan* 430074, *China*
2. *Disaster Prevention Research Institute* (*DPRI*), *Kyoto University*, *Kyoto* 612-8236, *Japan*

ABSTRACT: The mechanism involved in deep-seated landslide-debris flow disaster chains has been studied for many years, however, it is still not completely understood. This study aims to analyze the key factors that were involved and led to the geological disaster of Shaziba 62.0 m deep landslide-debris flow. Two extensive field investigations were conducted before and after the slope failure event. The study further used drilled cores, high-density resistivity method, and aerial photographs to obtain valuable insights into the disaster chain. It was found that opencast coal mining operations broke the locked segment of the front edge and heavy rainfall softened the slip zones along the faults. Mechanical calculations demonstrated that the coupling condition of the opencast coal mining and heavy rainfall triggered the landslide. A new evolution model was put forth to describe the complex mechanism of combining progressive retreat and tractive failure of hydraulic drive landslide, which was governed by the bedding-plane rock layer. Surface runoff caused the mass of the landslide to liquefy throughout the sliding process, resulting in overlapping deposits, debris-flow-barrier-lake, and erosion. These new insights led to the indication of a different triggering mechanism of landslides-debris flows, as well as laid the foundation for the proposed physical and mechanical mechanism model based on progressive retreat soil-rock mixed landslides with an upper locked segment and lower weak interlayer under heavy rainfall.
KEY WORDS: landslides, debris flow, progressive retreat landslide, evolution model, locked segment.

0 INTRODUCTION

Shallow landslides, debris flows, and other destructive natural hazards induced by heavy rainfall in mountainous regions are sometimes not independent but combined to form a disaster chain (Chen et al., 2021; Zhou et al., 2020; Hiraishi and Okura, 2017; von Ruette et al., 2016; Zangmo et al., 2009). Some of the documented large-scale landslide events include the Mount Meager rock slide-debris flow in Canada on August 6, 2010 (Guthrie et al., 2012), the Jiweishan rock avalanche-debris flow in China on June 5, 2009 (Tang et al., 2015), and the Shiban landslide-debris flow in China on July 8, 2020 (Yu et al., 2022). Rugged terrain, rivers, steep gorges, strong tectonic activities, strata characteristics, and heavy rainfall are other causes that commonly trigger slope failure (Summa et al., 2022; Conforti and Ietto, 2020). In addition to natural factors, human activity in recent decades has resulted in many slope failures (Tang et al., 2015). For instance, following the construction of the Three Gorges Dam on the Yangtze River, more than 3 800 disaster chains occurred along the banks of the reservoir (Tang et al., 2015; Fourniadis et al., 2007). The sources of the disaster chains are generally shallow soil landslides or rock landslides (Chen et al., 2022; Kang et al., 2022; Baselt et al., 2021; Agliardi et al., 2001; Broili, 1967).

However, the mechanism involved in deep-seated landslide-debris flow disaster chains is not well understood, due to their initiation and evolution process. The main concern is that the geological structure is not sufficiently characterized to investigate deep-seated landslides (Pánek et al., 2019; Kojima et al., 2015). Several rain-induced deep-seated catastrophic landslides occurred on sliding surfaces along faults, but the details about them remain uncertain and their potential locations have yet to be established (Arai and Chigira, 2018). Findings from Jones et al. (1991) also showed that shallow coal mining beneath slopes has been one of the main reasons for several deep-seated landslides. Coal mining operation is performed beneath mountainous or hilly terrain, which may lead to the subsequent roof collapse and trigger landslides (Yang et al., 2022; Riesgo Fernández et al., 2020; Fathi Salmi et al., 2017; Kataoka et al., 2017; Al-Shayea et al., 2000). It is well established knowledge that the roof of the coal seam is made of lime-

*Corresponding author: xu1963@cug.edu.cn
© China University of Geosciences (Wuhan) and Springer-Verlag GmbH Germany, Part of Springer Nature 2025

Manuscript received January 17, 2023.
Manuscript accepted March 28, 2023.

Chen Taiyi, Xu Guangli, Hiraishi Tetsuya, 2025. New Understandings of the Shaziba Landslide-Debris Flow in Hubei Province, China. *Journal of Earth Science*, 36(4): 1632–1649. https://doi.org/10.1007/s12583-023-1833-3. http://en.earth-science.net

stone due to coal-forming sedimentary environments (Chen et al., 2018; Li et al., 2018; Cai et al., 2011; Andrews et al., 1996; Isbell and Rubén Cúneo, 1996). However, the influence of coal mining activities on landslide formation has not been well investigated. Additionally, the damage energy of disaster chain caused by deep landslide is large and rather unexplored. Therefore, this necessitates the investigation of the characteristics and formation mechanism of deep-seated landslide-debris flow disaster chains (Wu et al., 2023; Zhou et al., 2020; Deng et al., 2019; Imaizumi et al., 2019; Tanyaş et al., 2019; Fan et al., 2018). This study attempts to analyze the key factors governing the evolution of slopes toward instability. The Shaziba landslide-debris flow event has been taken as the research background, based on which a physical and mechanical mechanism model is developed through field investigations, drilled cores, high-density resistivity method, aerial photographs and mechanical calculations.

1 THE SHAZIBA LANDSLIDE-DEBRIS FLOW

On July 21, 2020, a large-scale landslide-debris flow occurred in Mazhe Village, Tunbao Township, Enshi City, Hubei Province (Figures 1a and 1b). The landslide had a volume of 2 500 × 10^4 m^3, and about 144 × 10^4 m^3 of debris along the gully had slipped into the Qingjiang River, forming a barrier lake (Figure 1c). This landslide-debris flow resulted in the immediate evacuation of 1 399 people and block the provincial highway S233. Several houses, village roads, power facilities, and farmlands were destroyed. Although there were no casualties due to this event, often hazardous geological events pose a major threat to human lives and properties (Gong et al., 2021). After the event, the Shaziba landslide-debris flow has been reported and investigated by many researchers (Hu et al., 2022; Xue et al., 2022; Song et al., 2021). The studies concluded that the infiltrated rainwater increased the saturation level of the slope body, which reduced the shear strength of the soil below that of the *in-situ* soil. This resulted in crack formation in the slope body, which triggered the landslide and ultimately the failure. However, later investigations revealed that fractured rock blocks and coal were found in the study area.

To better understand the characteristics and formation mechanism of the Shaziba landslide-debris flow, two field investigations were conducted at the time of the landslide occurrence and after the landslide along with investigations using drilled cores and high-density resistivity method. These expeditions produced some new evidence that contradicts previous studies and reports. Data

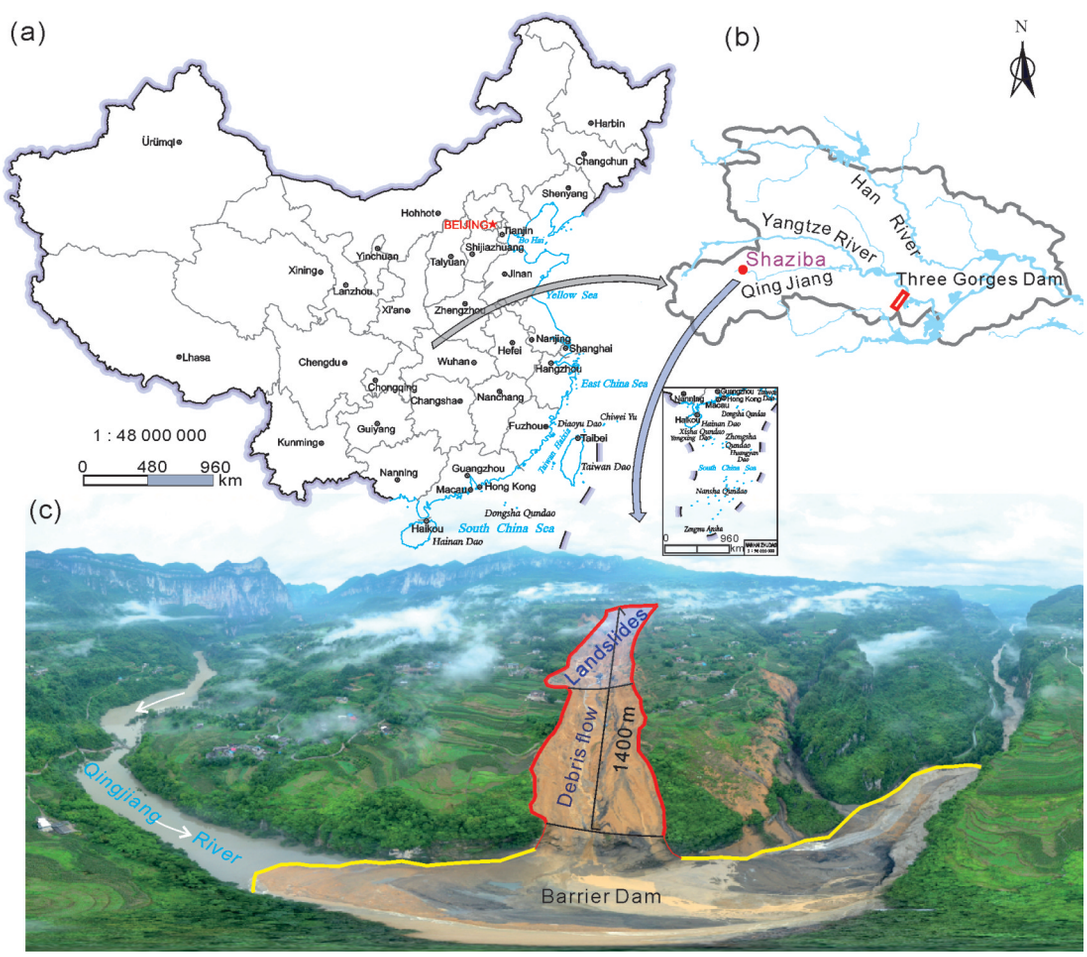


Figure 1. The Shaziba landslide-debris flow location map. (a), (b) Location of the Shaziba landslide (GS(2019)1673); (c) aerial image of landslide partially blocking the Qingjiang River, a tributary to the Yangtze River, in Enshi, Hubei Province.

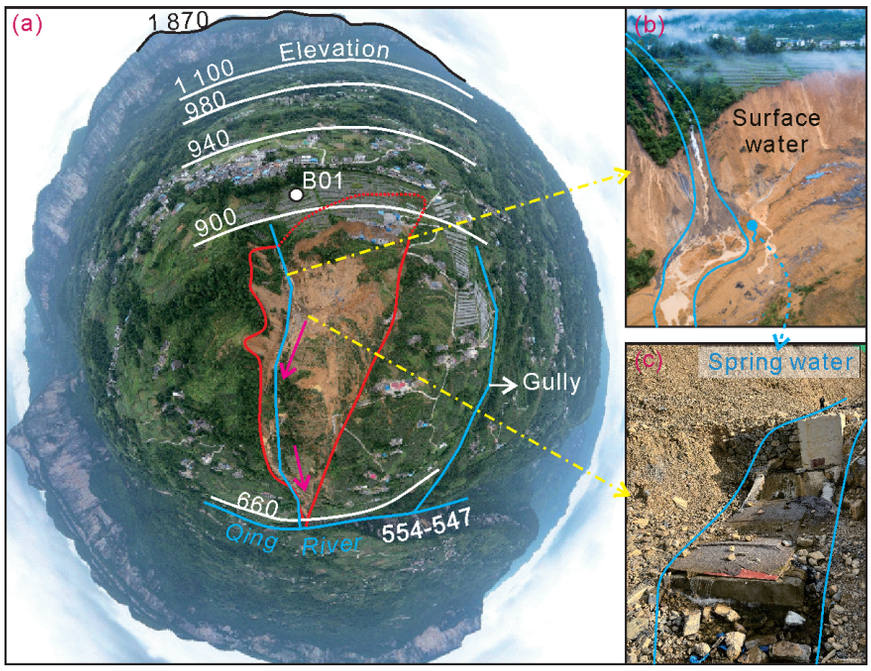


Figure 2. Topography and runoff. (a) Top view of the landslide topography and gully; (b) surface water of trailing edge of landslide; (c) spring water of trailing edge of landslide.

on human activities (opencast coal mining) and rock mass fracture were gathered to explore their roles in the triggering mechanism. Analysis and interpretation of field characteristics, as well as mechanical calculations and aerial photographs, allowed a more convincing explanation of the failure mechanism.

1.1 Geological and Stratigraphic Settings

Geologically, the Upper Permian Liangshan-Dalong Formation, which is made up of limestone interbedded with slate, sandstone, and coal seam, was the major outcropping formation (Cheng et al., 2021; Chen et al., 2018). The covering Quaternary silty clay layer was very thick (Hu et al., 2022; Song et al., 2021). The faults, anticline, and syncline were developed in regional background of the study area. Affected by faults, the rock mass was relatively broken and provided favorable conditions for the occurrence of geological disasters (Qin et al., 2010; Tang et al., 2010).

The region can be distinguished by an erosion canyon with deep incisions of valleys and steep cliff development (Figure 2a). The landslide occurred on the north bank of the Qingjiang River. The back edge of the landslide was under a gentle slope platform with an average slope angle of 5°, and the catchment area was 9.1 km^2 (Figure 2a). The landslide occurred in the lowest portion of the slope and was surrounded on all sides by natural gullies. The slope angle after the landslide was 10°. Surface water and spring water were developed. Figure 2a presents the geographical and topographical conditions of the gully. The inclinations of the slopes at both sides were very steep, which means rainfall was easily collected at the gully. The gully flood flow and spring flow are approximately 6.0 and 1.5 m^3/s, respectively (Figures 2b and 2c).

1.2 Precipitation

Based on Enshi Meteorological Station monitoring data retrieved from the National Meteorological Information Centre, Enshi experienced continuous heavy rainfall prior to the occurrence of the landslide (Hu et al., 2022; Song et al., 2021).

Comparing the summer rainfall data for the years 1954 to 2020, it was found that the rainfall in recorded in 1982 was higher than that in 2020 (Figure 3a). Furthermore, opencast coal mining operations were carried out from 1960 to 1980. Time series InSAR results showed that the central part of the slope body area has been several signs of displacement changes after heavy rainfall since the rainy season of 2018 (Xue et al., 2022). The amount of rainfall in a single day in 2018 was close to that in 2020 (Figure 3b). This information indicated that the central displacement occurred at the opencast coal mining location and a single day of heavy rainfall did not cause the whole landslide.

Record-setting consecutive rainfall occurred from 16 July to 17 July 2020, followed shortly by the 2020 landslide (Figure 3b). The rainfall suddenly decreased after the landslide started (Figure 3c). The daily rainfall recorded on July 16 was 64.8 mm, whereas, it was 155.8 mm on July 17. The landslide triggered by rainfall threshold was 240.1 mm, and the rainfall intensity was 8.0 mm/h (Figure 3d). These findings from the nearby Tunbao Meteorological Station, where the Shaziba landslide occurred, demonstrated that two days of intense rainfall rather than an extended period or a single day of precipitation caused the landslide.

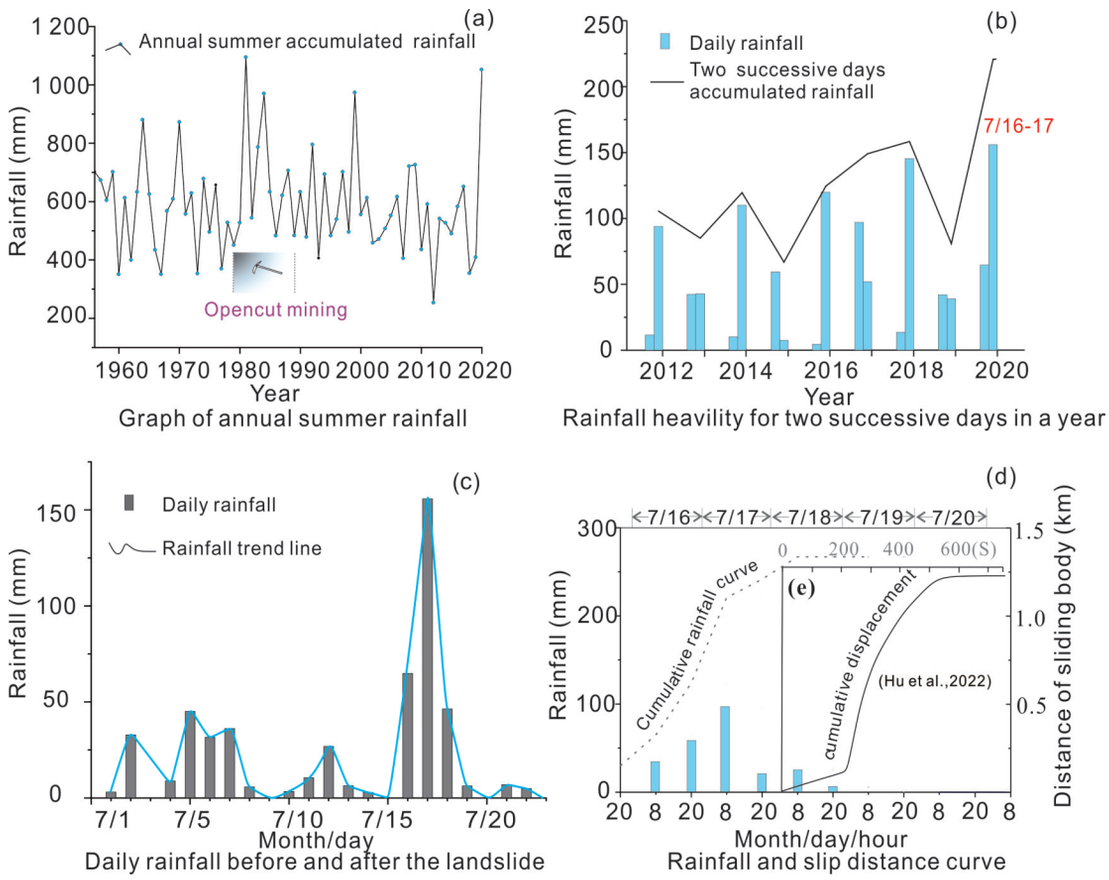


Figure 3. Rainfall statistics for the region. (a) Annual summer rainfall; (b) two successive days of heavy rainfall; (c) daily rainfall before and after the landslide; (d) rainfall per hour.

1.3 Features of The Shaziba Landslide-Debris Flow

Figure 4 shows the engineering geological features of the Shaziba landslide-debris flow surface. The elevation of the landslide front edge was 650–750 m, and the elevation of the trailing edge was 930–950 m. The landslide was 1 200–1 600 m long from north to south and 500–700 m wide from east to west. The thickness of the slip mass was 13–62 m with an area of 80 × 10^4 m^2 and a volume of 2 500 × 10^4 m^3. It was a large landslide of mixed rock and soil, with a main sliding direction of 200°.

The landslide region was primarily composed of clay, with a few boulders made of weathered colluvium of limestone. Due to the thick covering layer, no visible slip zone was detected when the landslide occurred (Hu et al., 2022; Cheng et al., 2021; Song et al., 2021).

2 ANALYSIS OF GEOLOGY AND TECTONIC STYLES

Rainfall is often the triggering factor for most geological disasters (Xue et al., 2022; Wasowski and Pisano, 2020; Wartman et al., 2016). Drilled cores and the high-density resistivity method were used to determine critical factors that may have participated in the landslide. Characteristic features of landslides can be partly revealed using drilled cores (Furuki and Chigira, 2019; Chigira et al., 2013; Wakizaka, 2013). The high-density resistivity method can provide spatial information about subsurface geological structures such as active faults and bedrock (Cheng et al., 2021; Pazzi et al., 2018; Yoshida et al., 2014).

2.1 Strata Combinative Characteristics

Figure 5a shows the strata in the sliding area to the north of the rear edge of the landslide. The thickness of surface clay in the exploration area was more than 8.0 m. The total thickness of the gravelly clay and gravel layer was up to 40.0 m. The thickness of the carbonaceous slate and coal seam was about 13.0 and 5.0 m, respectively. Figure 5b shows the strata in the sliding range of the landslide, revealing the absence of carbonaceous slate and the reduction of coal seam thickness. However, from the geological origin analysis, it was found that the coal seam roof was composed of limestone (Chen et al., 2018; Li et al., 2018; Cai et al., 2011; Andrews et al., 1996; Isbell and Rubén Cúneo, 1996; Chen, 1989). It was initially determined through the comparison of geologic boreholes that the limestone was the sliding bed and the coal seam was the sliding zone.

The surface clay was a thick impermeable layer with a low permeability coefficient of 4.82 × 10^{-5}–5.06 × 10^{-5} cm/s established through laboratory penetration tests. It was difficult for the rainwater to infiltrate the slope in a short time. Furthermore, no groundwater was found in

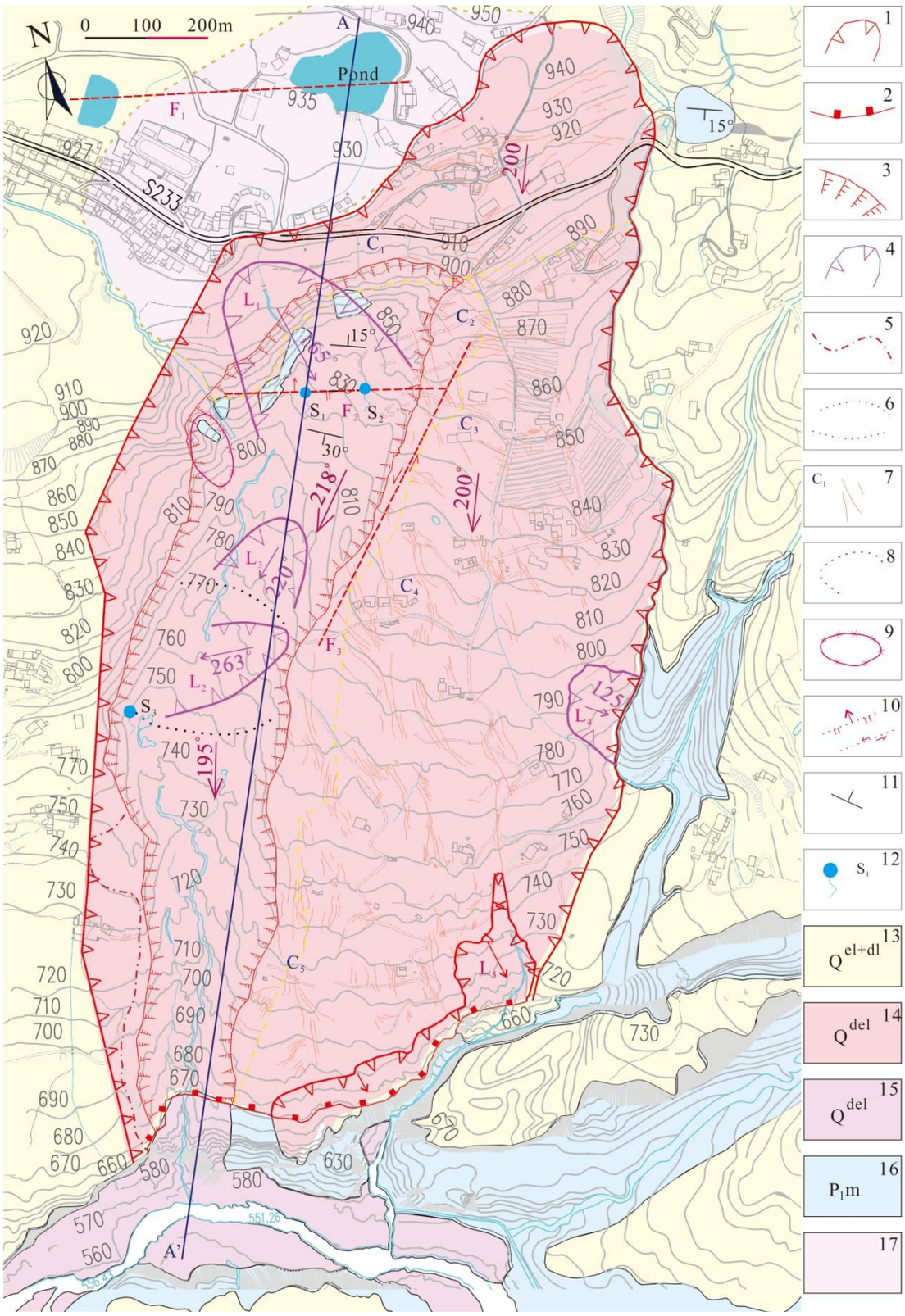


Figure 4. Topography and surface geology of Shaziba landslide-debris flow. 1. The landslide boundary; 2. the landslide front line; 3. the landslide groove steep wall; 4. the overlap range line; 5. coal mining area; 6. fissure; 7. sphere of influence; 8. attitude of rock formation; 9. spring water; 10. Quaternary eluvial and deluvial soils; 11. landslide deposits; 12. barrier lake; 13. Lower Permian Maokou-Gufeng Formation limestone; 14. landslide affected area; 15. borehole number and location; 16. residential buildings; 17. surface water.

the geological boreholes. In order to understand how precipitation infiltrates into the slip zone and identify underground structures, the high-density resistivity method was used in the study area.

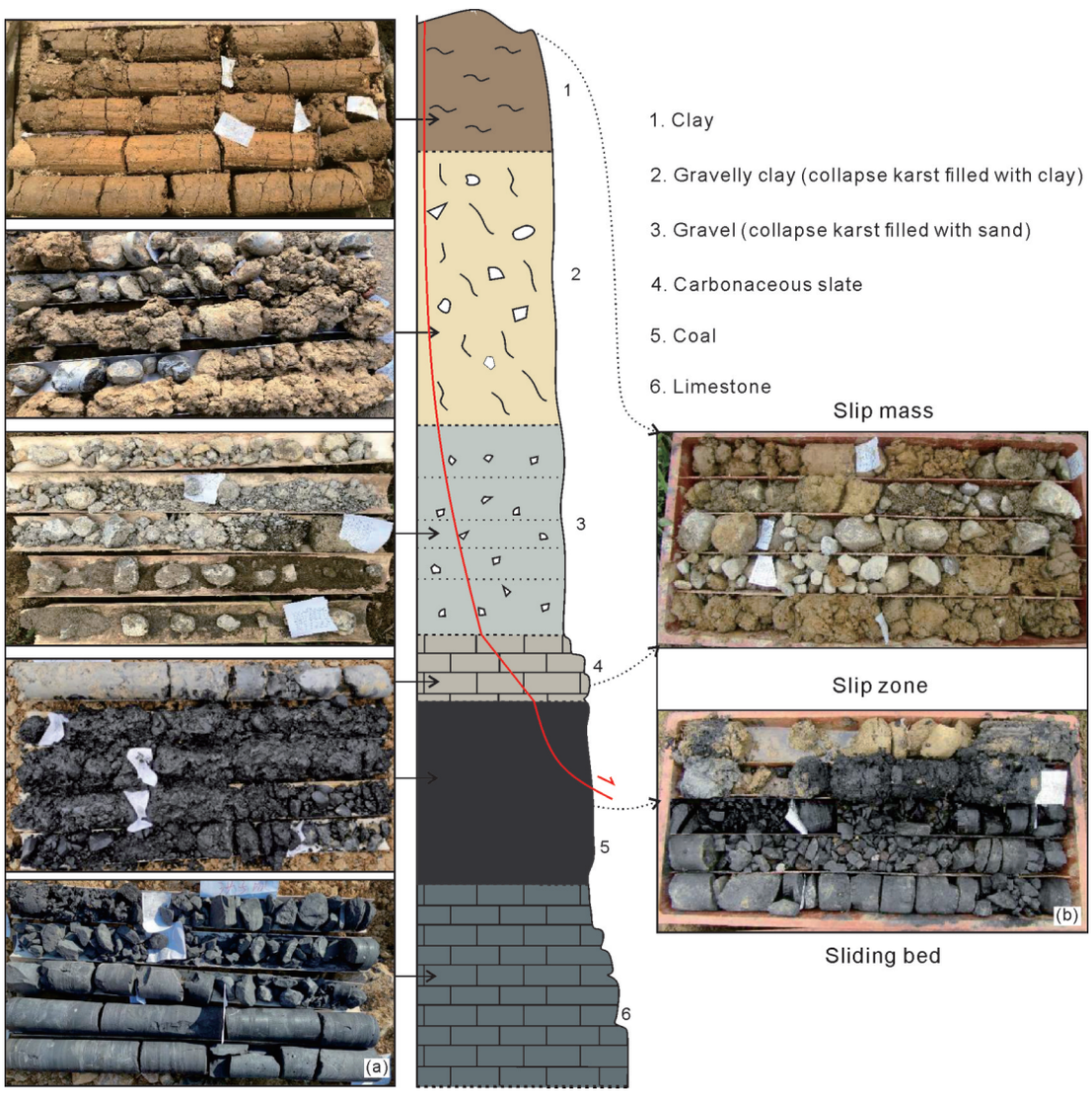


Figure 5. Geology columnar section (in Figure 4). (a) B01 in the area without landslide; (b) B04 in the middle part of the landslide.

2.2 Tectonic Characteristics

Figure 6 shows the schematic diagram of the Wenner-α array measurement. For the homogeneous and isotropic half-space medium, the apparent resistivity ρ_s in ohm-meter ($\Omega \cdot m$) was calculated using Ohm's law expressed as Eq. (1) and Eq. (2) (Yang et al., 2020; Yin et al., 2020; Caterina et al., 2013; Loke and Barker, 1996, 1995).

$$\rho_s = \frac{KU_{MN}}{I} \tag{1}$$

$$K = 2\pi / \left(\frac{1}{AM} - \frac{1}{AN} - \frac{1}{BM} + \frac{1}{BN} \right) \tag{2}$$

where U_{MN} is the measured potential difference in mV, I is the supplied current in mA, and K is the geometric factor with respect to electrode spacing.

The background resistance value of subsurface limestone was greater than 500 $\Omega \cdot m$. The resistance of coal seams and faults was 10 – 50 $\Omega \cdot m$, whereas the resistance of clay was 30–100 $\Omega \cdot m$. The resistance of gravelly soil was 50 – 500 $\Omega \cdot m$, wherein the resistance increased with the increase in the block stone content). Profiles in Figure 7 demonstrate a strong contrast in resistivity with underlying sedimentary layers, allowing for the precise identification of fault position, bedrock surface geometry, and coal seam distribution. Resistivity profiles of 1–5 revealed a fault passing the pond at the trailing edge of the landslide. More details on the fault can be found in Cheng et al. (2021). Resistivity profiles of 6 – 8 and 10–12 showed that coal seams in the landslide groove area were exposed. The profiles obtained through high density resistivity test provided a convincing proof of the presence of coal seams outcropping.

3 EVIDENCES OF ROCK MASS FRAGMENTATION

The slip surface is sometimes not sampled due to its softness, so it flows out during drilling (Wakizaka, 2013). The interpretation of geophysical images obtained from the study area was limited. Outcrop observations, on the other hand, provide much wider information (Furuki and Chigira, 2019). Two field investigations in unprecedented detail were conducted both during and after the landslide

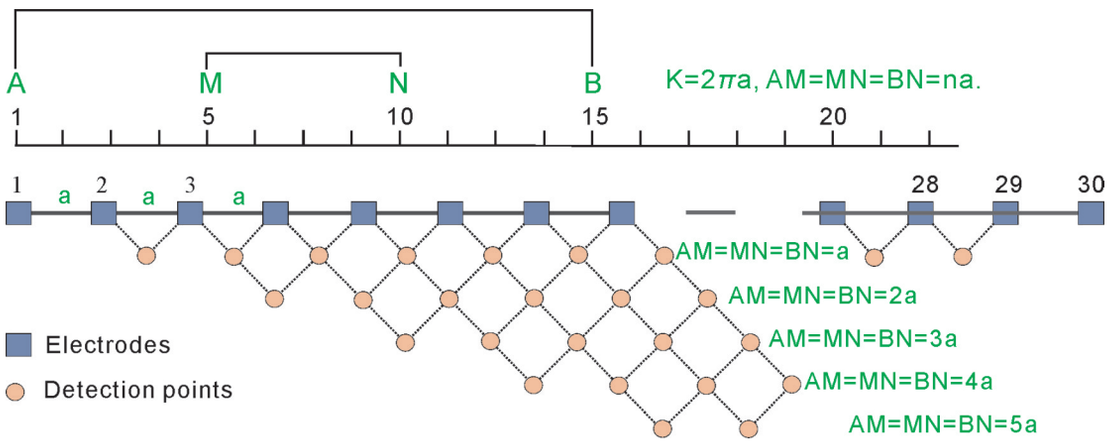


Figure 6. Schematic diagram of Wenner-*α* array measurement.

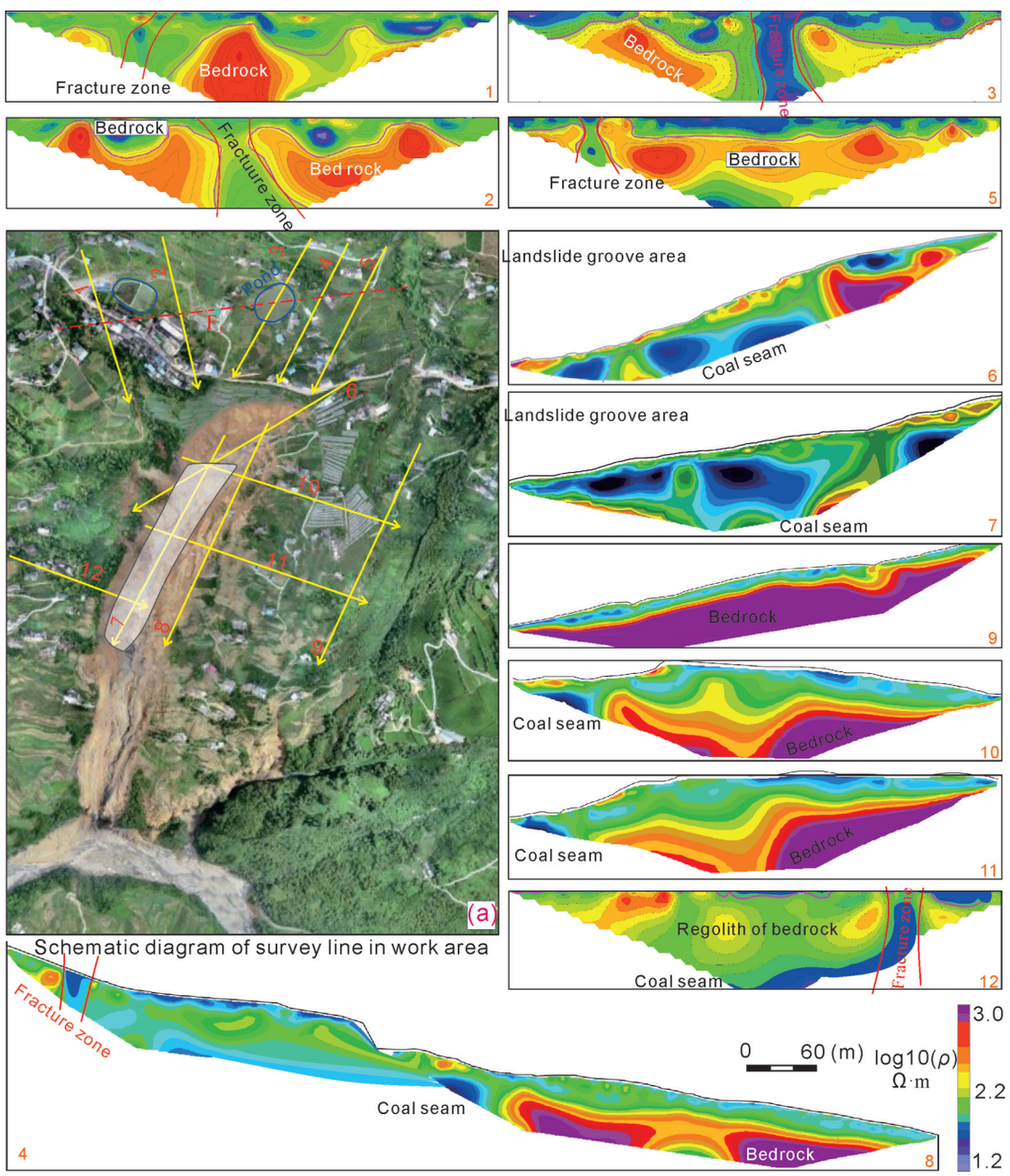


Figure 7. Resistivity profiles of the measuring lines with different colors representing different electrical resistivity.

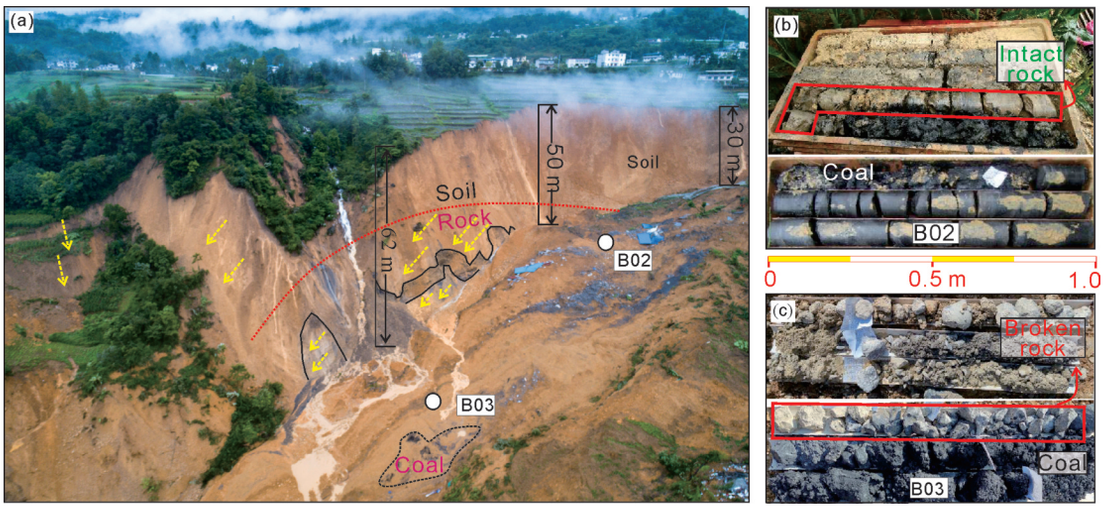


Figure 8. Field investigation in July 2020. (a) Characteristics at the trailing edge of the landslide; (b) cores drilled near the pure soil landslide scarp; (c) cores drilled near the soil-rock landslide scarp.

to develop a physical model of the Shaziba landslide-debris.

3.1 New Phenomena at the Trailing Edge of the Landslide

The first field investigation was carried out in July 2020 (Figure 8). Due to the thick coverage of the sliding body, no visible slip zone was found. Figure 8a shows the landslide scarp of the rock stratum and soil layer, which was thicker than a single pure soil layer. The carbonaceous slate close to the soil side was discovered to be intact through the emergency geological boreholes B02 and B03 near the landslide scarp, while that close to the soil-rock composite side was broken (Figures 8b and 8c).

The second field investigation was carried out in October 2022 (Figure 9). The rock mass fracture surface and the sliding surface of the landslide scarp are clearly found plainly visible due to the sliding mass moved by nature and human activities.

Fault breccia and rock surface scratch were observed in the images (Figure 9a). The direction of rock surface scratch and rock mass bedding were found to be consistent with that of joints and slipping (Figures 9b and 9c). Tension fracture section and joint of rock mass seemed to be a common phenomenon in bottom part at the trailing edge of the landslide (Figures 9d and 9e). These outcrops exposed the presence of interlayer slip and rock mass fracture, thus proving that the 62 m deep landslide was not a pure soil landslide but instead was triggered by an existing fault.

3.2 Analysis of the Lithology

In order to determine the cause of the rock fracture and slip, the lithology was analyzed. The lithological association was mainly composed of carbonaceous slate and limestone interbedding, with schistosity belts forming within the carbonaceous slate and mudstone intercalation developing in the limestone. The direction of the formation was consistent with the bedding (see Figure 10).

As can be seen from Figure 10a and Figure 10b, the schistose carbonaceous slate intercalation developed in the limestone, which then was exposed on the sliding surface of rock mass (Figure 10c). Figure 10d and Figure 10e show mudstone intercalation developed in limestone. Its fragmented form can be seen in Figure 10f. The schistose carbonaceous slate and mudstone intercalation caused weak interlayer sliding of the rock mass. The rock mass easily separated along the interlayer and was fragmented, proving that the mechanical characteristics of the weak interlayer deteriorated with wetting-drying cycles in the course of natural conditions from July 2020 to October 2022.

3.3 Characteristics of Disaster Chain

A detailed investigation of the slip surface was carried out along the sliding direction of the landslide (Figure 11). First, a large number of rock stratum tension cracks appeared on the west side at the trailing edge of the landslide, while only pure soil landslide occurred on the east side as the height of the trailing edge decreased. Second, the limestone sheared at the bottom of the landslide, exposing the coal seam. Third, the limestone slid along the coal seam, resulting in crushing and cracking. Fourth, the coal seam was pushed over the Quaternary clay, and the strata appeared in reverse order phenomenon. Fifth, the phenomena of the scraping effect occurred with the flow of debris, and the maximum depth of erosion was 12.0 m. Finally, slipped mass flowed into Qingjiang in a liquid state to form a landslide-debris flow-barrier lake-disaster chain.

The coal seam was the slip zone on the southern side of the fault. Under the influence of steep surface, the schistose carbonaceous slate and mudstone intercalation became the slip zones of rock mass and drove the overall slip of the overburden soil on the northern side of the fault.

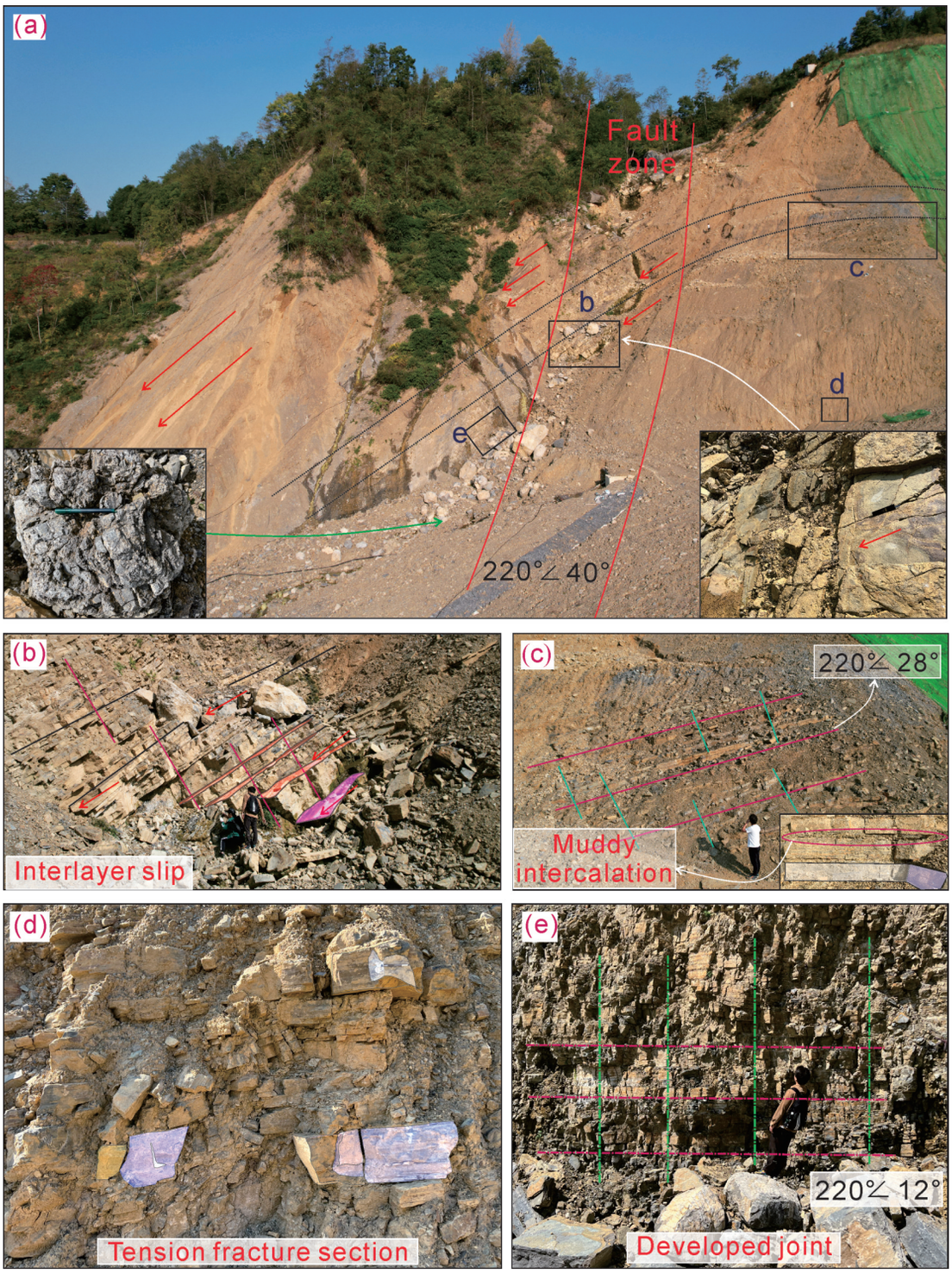


Figure 9. Field investigation in October 2022. (a) Characteristics at the trailing edge of the landslide; (b) interlayer slip of rock mass; (c) muddy intercalation in middle part; (d) tension fracture section of rock mass in bottom part; (e) developed joint of rock mass in bottom part.

Combined with the investigations, drilled cores, high-density resistivity method and aerial photographs, the accurate geological profile of *A*–*A*' (specific location can be seen in Figure 4) is shown in Figure 12.

4 FAILURE MECHANISM OF DISASTER CHAIN

4.1 Initiation

Before sliding, the source area was affected by human activities (opencast coal mining). According to the aerial pictures obtained from June 15 to July 21, 2020 (Figures 13a–13c), the landslide seemed to be a progressive destruction. The initiation location was found to be the opencast mining coal area which was consistent with the description of witnesses (Figure 13e). In the case of heavy rainfall, F_2 provided an infiltration softening slip channel for the surface runoff. In addition, the pond water

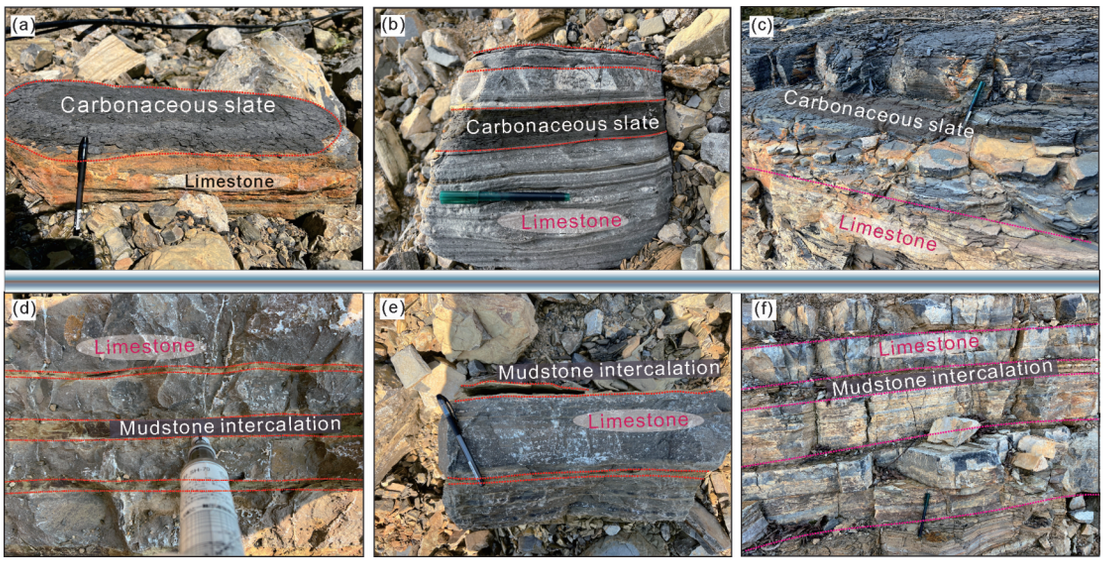


Figure 10. The characters of lithology. (a), (b) The schistose carbonaceous slate intercalation in limestone of landslide deposition; (c) the schistose carbonaceous slate on slip surface; (d), (e) the mudstone intercalation in limestone of landslide deposition; (f) the mudstone intercalation of lateral tension surface of landslide.

level dropped significantly in the early stage of the landslide and finally, it dried out (Figure 13d), which proves that fresh cracks occurred under the influence of deformation, leading to the connection path between fault F_1 and the pond. This indicates that the initiation of the disaster chain was triggered by both human activities and rainfall factors.

In order to quantitatively analyze landslide initiation, *in-situ* test and laboratory test were carried out to obtain the shear strength parameters. The rigid limit equilibrium inversion analysis was to verify the mechanical property of coal. *In-situ* test, laboratory test and Hoek-Brown criterion were to evaluated the mechanical property of rock mass. Details of tests are shown in Figure 14.

Through the tests and analysis, the parameters were obtained in Table 1.

Under the action of groundwater, the slope stability coefficient can be expressed (Zhang et al., 2020; Vassallo et al., 2015; Bi et al., 2012),

$$F_s = \frac{(W\cos\alpha - U - V\sin\alpha)\tan\phi + cL}{W\sin\alpha + V\cos\alpha} \quad (3)$$

$$W = \gamma A \quad (4)$$

$$U = \frac{1}{2}\gamma hL \quad (5)$$

$$V = \frac{1}{2}\gamma h^2 \quad (6)$$

where F_s is the safety factor, W is the weight of the landslide, U is the uplift pressure along the sliding surface, V is the hydrostatic pressure along the tension crack, α is the dip angle of the slip surface, φ is the internal friction angle of the sliding surface, c is the cohesion of the sliding surface, and L is the length of the sliding surface along the sliding direction.

L = 200 m and h = 20 m are based on the initiation stage of the landslide (Table 1, the mechanical parameters were obtained by shear test). Under the varying conditions, the calculating results of F_s by Eq. (3)–Eq. (6) are

The initial stage of a landslide happened as a result of the coupled conditions of opencast coal mining and heavy rainfall.

In order to simulate slope stability under excavation and rainfall conditions, we carried out finite element calculation by FLAC 3D (Figures 15 and 16). The physical model is shown in Figure 15a. Figures 15b and 15c demonstrate the landslide was divided into four parts and the zone of maximum shear strain increment was consistent with the location of coal and carbonaceous slate. Figure 16a shows the state of shear and tension. The landslide has four tension concentration zones. The maximum shear principal stress occurred in the slip zone (see in Figure 16b). The maximum displacement of the landslide occurred at the upper of the slip zone (see in Figure 16c). The stress and displacement of simulation were approximate to the actual slope failure process (see in Figures 15, 16 and 17b).

The primary cause of the rock mass' sliding and fracture along the carbonaceous slate and mudstone intercalation under the influence of F_2 was the infiltration of surface runoff, which softened the coal seam. Due to the presence of a rock stratum above the slip zone, the landslide started to slide after the rock stratum was broken. Affected by the terrain and the occurrence of rock strata, the bedding soil-rock mixed landslide was formed.

4.2 Evolution Stage and Process

The landslide had slipped four times, with the first three slip zones being coal seams and the final slip zone being carbonaceous slate (Figures 17a and 17b). The slip zones of the landslide affected by the fault were different. The first three slip zones on the southern side of the

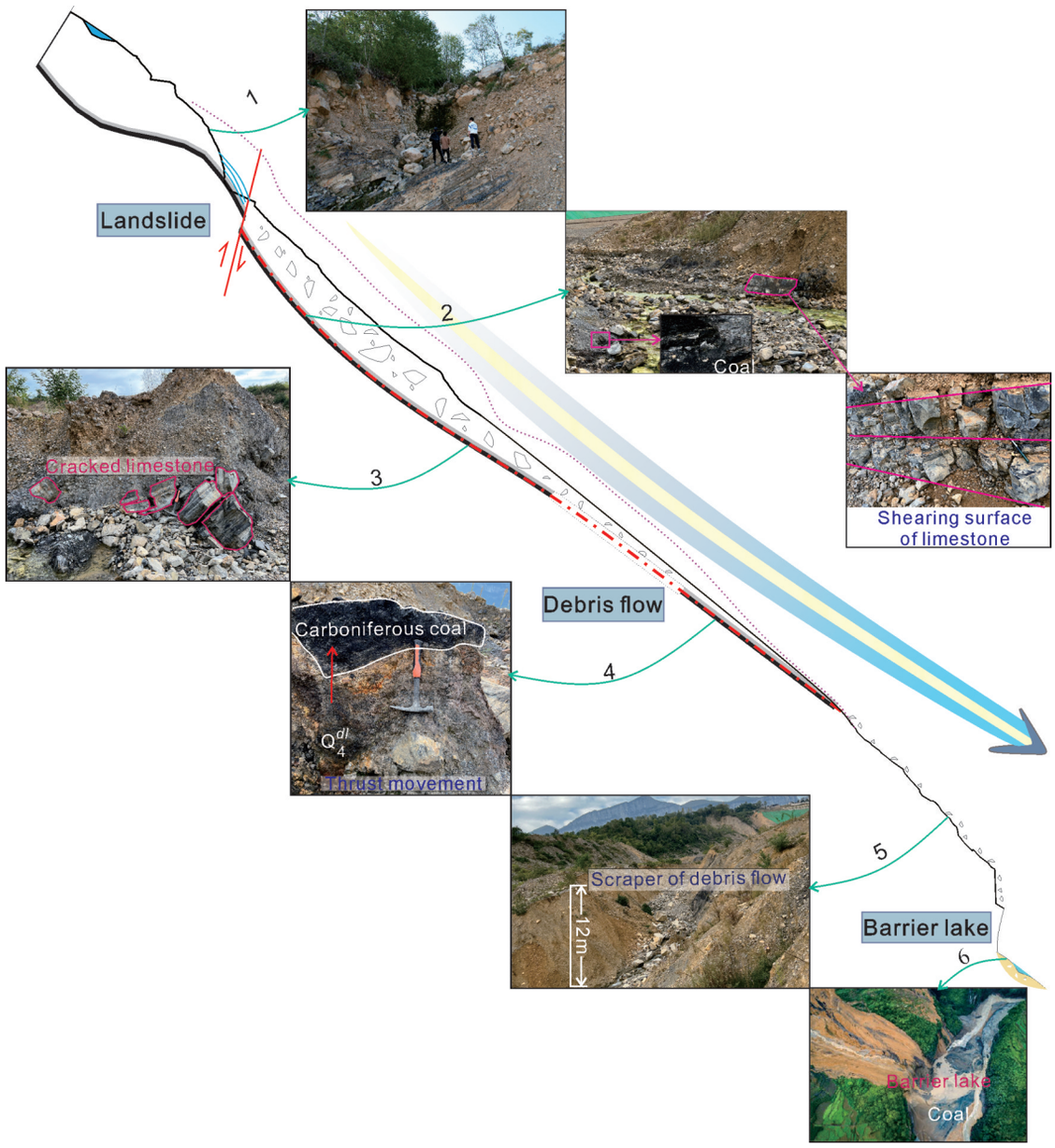


Figure 11. Characteristics of disaster chain.

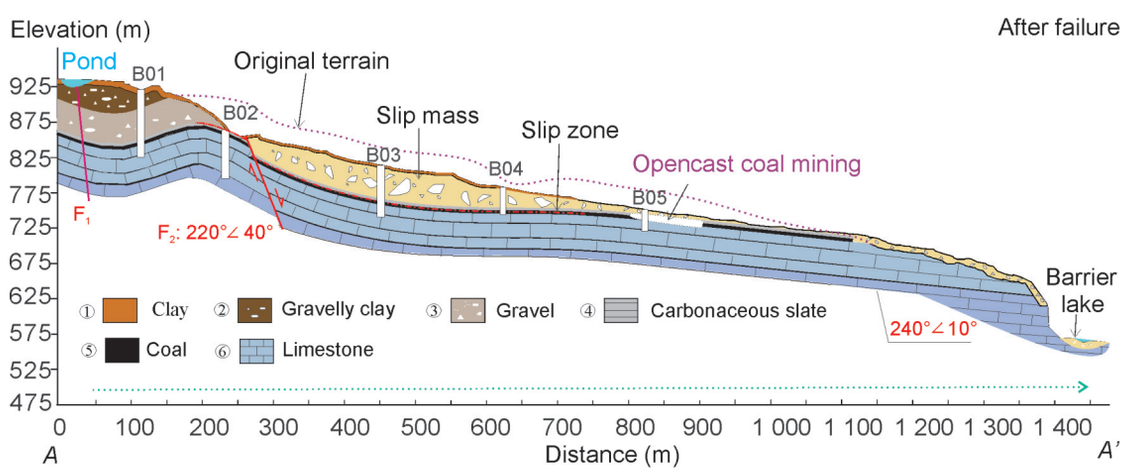


Figure 12. Geological profile (*A*–*A*').

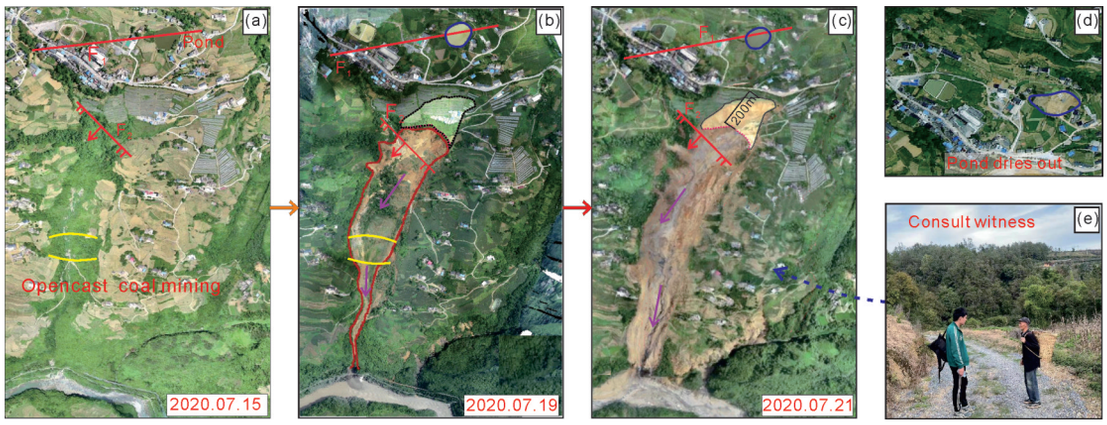


Figure 13. The sliding process of the landslide. (a) Aerial photograph before the landslide on July 15, 2020; (b) aerial photograph during the landslide process on July 19, 2020; (c) aerial photograph after the landslide on July 21, 2020; (d) the pond dries out; (e) consult witnesses about the process of landslide and opencast mining coal (Enshi Natural Resources and Planning Bureau).



Figure 14. *In-situ* test, laboratory test. (a), (b) Compressive strength of carbonaceous slate and limestone; (c), (d) direct shear test of mudstone intercalation in limestone; (e), (f) direct shear test of coal.

Table 1 Parameter value for calculation

Geomaterial	γ (kN/m^3)	c (kPa)	φ (°)
Overlaying soil	18.6	38.7	13.5
Coal	18.4	Nature: 29.8; Saturation: 23.5	Nature: 10.2; Saturation: 7.8

Table 2 Calculating results of F_s

Conditions	F_s
Opencast coal mining	1.62
Heavy rainfall	1.31
Opencast coal mining + Heavy rainfall	0.98

fault were carbonaceous slate, and the last slip zone on the northern side was the coal seam. Since the trailing edge of the landslide was located at the core of the anticline, it was a reverse-dip rock slope and the retreat failure was over temporarily. The evolution mechanisms of the Shaziba landslide-debris flow are shown in Figure 17.

After the landslide started, due to the rainwater infiltration, the landslide mass mixed with the surface runoff in the valley, thus increasing the pore water pressure in the landslide mass. This also resulted in a decrease in the soil shear strength and local shear failure of the soil mass. Tensile and shear cracks in the slope soil mass were also formed, and the original cracks and pores expanded in the soil mass. Rainwater infiltration increased the pore water pressure of these fissure-saturated soils to increase the hydrostatic pressure and uplift pressure. The shear failure area expanded and connected to form a shear surface. With the rise in the fracture water level at the trailing edge of the slope, confined water in the slope body was characterized by the evolution characteristic of a triangle with low forwards and high backward. When the shear stress on the shear failure surface ex-

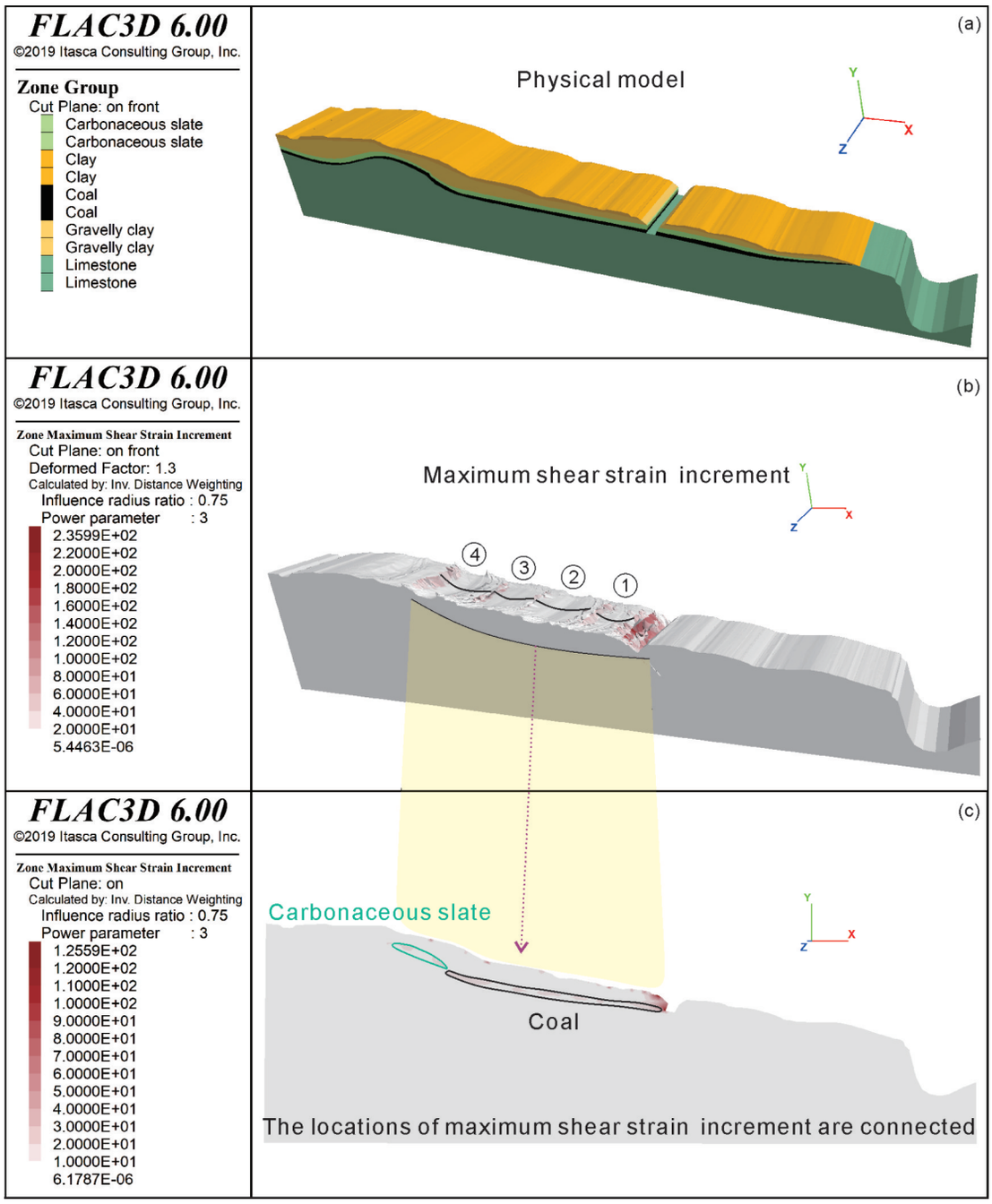


Figure 15. Finite element calculation. (a) Physical model of the landslide; (b), (c) maximum shear strain increment distribution of the landslide.

ceeded the shear strength, the rock and soil mass on the slope began to slide. The failure mechanism is shown in Figure 17c focusing particularly on the generation of hydrostatic pressure and uplift pressure under intense rainfall conditions and the corresponding deformation and failure processes.

Gravelly clay and clay are beneficial to lubrication and liquefaction. Which provided the material foundation for the formation of debris flow. And that the terrain of gully, the first sliding body blocked the drainage channel, resulting in the first temporary barrier lake. Subsequently, the water level gradually rises along with the terrain, softening the slip zone and causing the second sliding body to slide again, gradually forming a progressive retreat landslide (see in Figures 17a and 17b). Because of the large catchment area of the platform at the trailing edge of the landslide, the temporary barrier lakes on the landslide has broken. It then started to flow downslope, creating a debris flow. In the process of sliding, the sliding soil mass collided, peeled, and disintegrated (Zhou Z et al., 2020; Zhou S Y et al., 2019; Chen et al., 2018; Xu G L et al., 2015; Xu Q et al., 2010).

After the formation of the debris flow, the saturated fine-grained soil layer at the bottom of the valley in the circulation area and the ponding in the depression were continuously scraped, which caused the moisture content

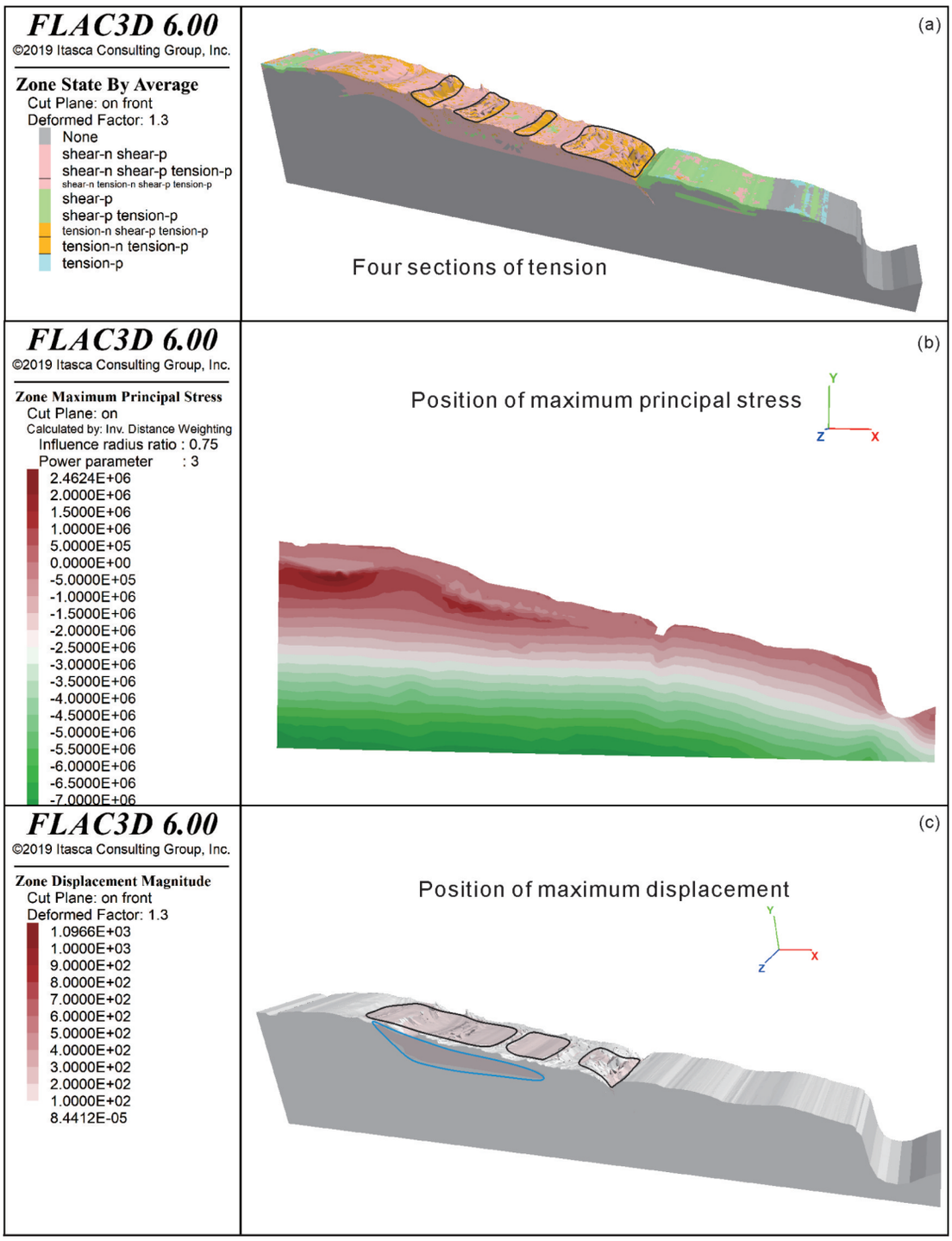


Figure 16. Finite element calculation. (a) Zone state of shear and tension; (b) maximum shear principal stress of the landslide; (c) maximum displacement of the landslide.

of the soil to continue to rise during the movement until it reached a saturation state. It finally flowed into the river in a liquid state to form a barrier lake. Due to the large volume and fast sliding of the landslide mass, the debris flow created overburden at the contraction of the topographic gully.

5 DISCUSSION AND CONCLUSION

Previous studies concluded that the direct triggering factor was heavy rainfall (Hu et al., 2022; Xue et al., 2022; Song et al., 2021). However, the original clay of the deep-seated landslide was thick, which is not conducive to rainfall infiltration. This study found that the catchment area of the platform at the trailing edge of the landslide was large and F_2 provided an infiltration softening channel for the surface runoff. Additionally, earlier research studies did not address the opencast coal mining or rock mass fracture. This paper puts forward different

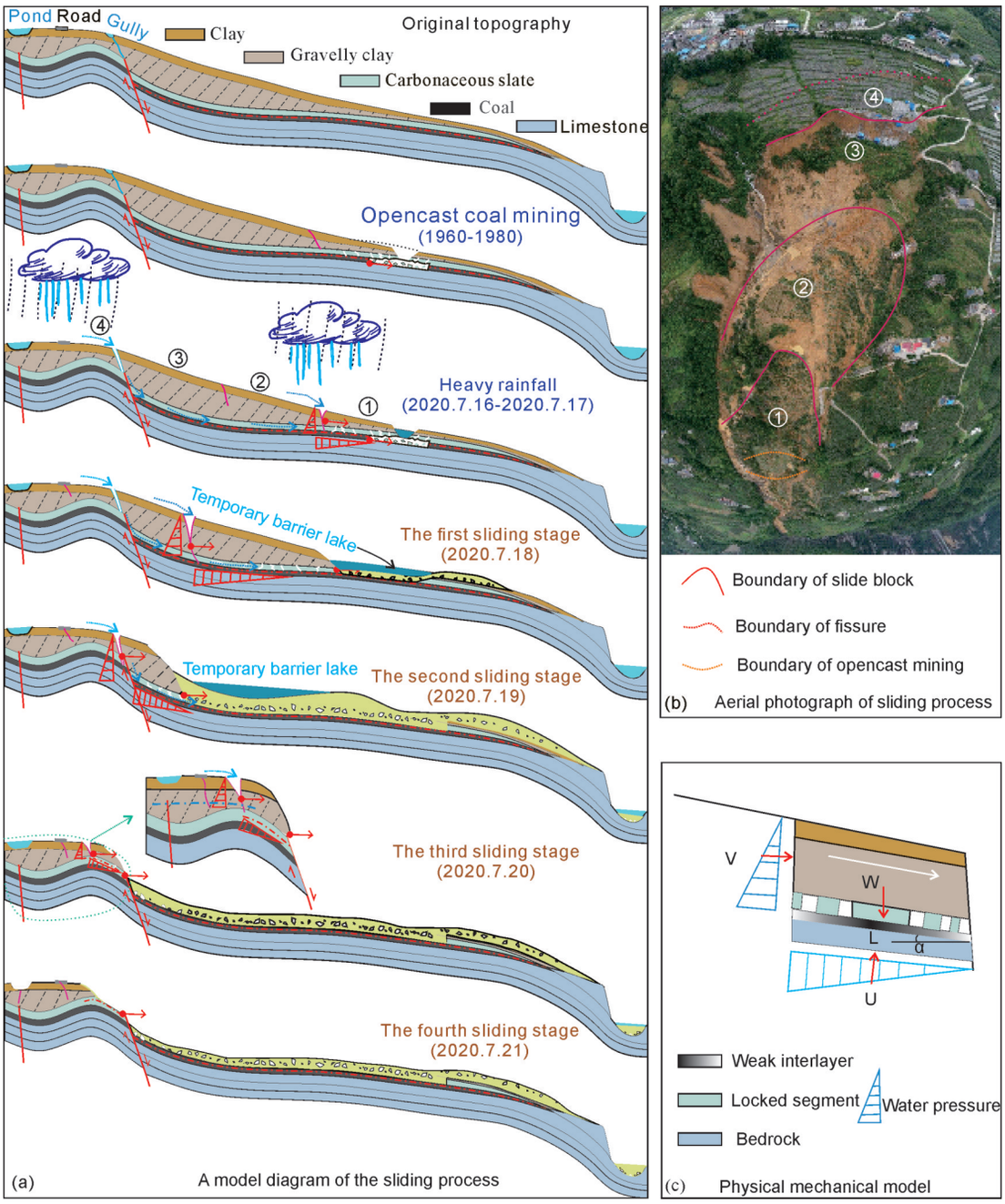


Figure 17. Evolution model of disaster chain. (a) Model diagram of section *A*–*A*' in Figure 4; (b) the sliding process based on aerial photograph; (c) physical mechanical model.

understandings of the formation mechanism of disaster chains.

Based on two detailed field investigations before and after the event, drilled cores, high-density resistivity method, aerial photographs and finite element analysis, it can be concluded that the Shaziba landslide-debris flow was resulted from a combination of past opencast coal mining, rainfall infiltration, faults, characteristics of rock and soil, terrain of gully and weak intercalated layers. The slip zones varied depending on the faults and rock. The slip zone on the south of the fault was coal seam, and that on the north of the fault was carbonaceous slate. The results of this study indicate that different materials and positions of single-layer slip zone may also exist in the landslide. This type of slip zone differs from the previous single layer and multi-layer slip zones, which is of great significance to the study of landslide mechanisms.

A new evolution model was proposed to describe the complex mechanism of combining progressive retreat and tractive failure of hydraulic drive landslide, which is controlled by the bedding-plane rock layer (Figure 17a). An evolutionary model for softening the slip zone and sliding process of the deeply seated landslide-debris flow disaster chain was developed. Lastly, a physical and mechanical mechanism model based on a translational soil-rock mixed landslide with an upper locked segment and

lower weak interlayer under heavy rainfall was proposed (Figure 17c).

The present study did not investigate the full mechanism of the establishment of the disaster chain. The overall mechanical calculation of landslides and detailed mechanism of debris flow formation will be summarized in a future study.

The findings of the study conducted on the Shaziba landslide-debris flow may lead to a contribution to the scientific understanding of landslide-debris mechanisms.

ACKNOWLEDGMENTS

The work was funded by the Key Research and Development Project of Hubei Province (No. 2021BCA219). The authors wish to thank the Hubei Investigation Institute of Hydrogeology and Engineering Geology, Jinzhou 434020, China for providing valuable data. The authors also express their sincere appreciation to the Enshi Natural Resources and Planning Bureau, Enshi 445000, China. The final publication is available at Springer via https://doi.org/10.1007/s12583-023-1833-3.

Conflict of Interest

The authors declare that they have no conflict of interest.

REFERENCES CITED

Agliardi, F., Crosta, G., Zanchi, A., 2001. Structural Constraints on Deep-Seated Slope Deformation Kinematics. *Engineering Geology*, 59(1/2): 83 – 102. https://doi. org/10.1016/S0013-7952(00)00066-1

Al-Shayea, N. A., Khan, K., Abduljauwad, S. N., 2000. Effects of Confining Pressure and Temperature on Mixed-Mode (I – II) Fracture Toughness of a Limestone Rock. *International Journal of Rock Mechanics and Mining Sciences*, 37(4): 629–643. https://doi.org/10.1016/S1365-1609(00)00003-4

Andrews, W. M., Hower, J. C., Ferm, J. C., et al., 1996. A Depositional Model for the Taylor Coal Bed, Martin and Johnson Counties, Eastern Kentucky. *International Journal of Coal Geology*, 31(1/2/3/4): 151 – 167. https://doi. org/10.1016/S0166-5162(96)00015-8

Arai, N., Chigira, M., 2018. Rain-Induced Deep-Seated Catastrophic Rockslides Controlled by a Thrust Fault and River Incision in an Accretionary Complex in the Shimanto Belt, Japan. *Island Arc*, 27(3): e12245. https://doi.org/10.1111/iar.12245

Baselt, I., Queiroz de Oliveira, G., Fischer, J. T., et al., 2021. Evolution of Stony Debris Flows in Laboratory Experiments. *Geomorphology*, 372: 107431. https://doi. org/10.1016/j.geomorph.2020.107431

Bi, R. N., Ehret, D., Xiang, W., et al., 2012. Landslide Reliability Analysis Based on Transfer Coefficient Method: A Case Study from Three Gorges Reservoir. *Journal of Earth Science*, 23(2): 187–198. https://doi.org/10.1007/s12583-012-0244-7

Broili, L., 1967. New Knowledges on the Geomorphology of the Vaiont Slide Slip Surfaces. *Felsmechanik and Ingenieurgeologie*, 5: 38–88

Cai, H. A., Li, B. F., Shao, L. Y., et al., 2011. Sedimentary Environments and Coal Accumulation Patterns of the Lower Cretaceous Shahai Formation in Fuxin Basin, Liaoning Province. *Journal of Palaeogeography*, 13(5): 481–491 (in Chinese with English Abstract)

Caterina, D., Beaujean, J., Robert, T., et al., 2013. A Comparison Study of Different Image Appraisal Tools for Electrical Resistivity Tomography. *Near Surface Geophysics*, 11(6): 639–658. https://doi.org/10.3997/1873-0604.2013022

Chen, S. Q., 1989. Characteristics of Tectonically Deformed Permian Coal in Hubei, Hunan, Guangdong and Guangxi Provinces and Analysis of Its Origin. *Journl of China Coal Society*, 14(4): 1–10, 113–116 (in Chinese with English Abstract)

Chen, T. Y., Wei, Q. R., Zhou, J. Y., et al., 2018. Sedimentary Epoch and Depositional Environment of Yunzhug Formation in Gamba-East Asia Area, Tibet. *Earth Science*, 43(8): 2893–2910 (in Chinese with English Abstract)

Chen, T. Y., Xu, G. L., Li, J. F., et al., 2022. Interaction Mechanism between Formation Process of Bank Collapse Disaster Chain and Territorial Space Utilization of Large Reservoirs. *Journal of Geoscience and Environment Protection*, 10(5): 160–169. https://doi.org/10.4236/gep.2022.105012

Chen, Z., Zhou, H. F., Ye, F., et al., 2021. The Characteristics, Induced Factors, and Formation Mechanism of the 2018 Baige Landslide in Jinsha River, Southwest China. *Catena*, 203: 105337. https://doi.org/10.1016/j.catena.2021.105337

Cheng, H. M., Xu, D. L., Wang, S., 2021. Application of Geophysical Prospecting in Emergency Response to Landslide Disaster: A Case Study of Shaziba Landslide in Enshi, Hubei. *Chinese Journal of Engineering Geophysics*, 18(2): 273–283 (in Chinese with English Abstract)

Chigira, M., Hariyama, T., Yamasaki, S., 2013. Development of Deep-Seated Gravitational Slope Deformation on a Shale Dip-Slope: Observations from High-Quality Drill Cores. *Tectonophysics*, 605: 104–113. https://doi.org/10.1016/j.tecto.2013.04.019

Conforti, M., Ietto, F., 2020. Influence of Tectonics and Morphometric Features on the Landslide Distribution: A Case Study from the Mesima Basin (Calabria, South Italy). *Journal of Earth Science*, 31(2): 393–409. https://doi.org/10.1007/s12583-019-1231-z

Deng, J. H., Gao, Y. J., Yu, Z. Q., 2019. Analysis on the Formation Mechanism and Process of Baige Landslides Damming the Upper Reach of Jinsha River, China. *Advanced Engineering Sciences*, 51(1): 9–16 (in Chinese with English Abstract)

Fan, X. M., Zhan, W. W., Dong, X. J., et al., 2018. Analyzing Successive Landslide Dam Formation by Different Triggering Mechanisms: The Case of the Tangjiawan Landslide, Sichuan, China. *Engineering Geology*, 243: 128–144. https://doi.org/10.1016/j.enggeo.2018.06.016

Fathi Salmi, E., Nazem, M., Karakus, M., 2017. Numerical Analysis of a Large Landslide Induced by Coal Mining Subsidence. *Engineering Geology*, 217: 141 – 152. https://doi. org/10.1016/j.enggeo.2016.12.021

Fourniadis, I. G., Liu, J. G., Mason, P. J., 2007. Landslide Hazard Assessment in the Three Gorges Area, China, Using ASTER Imagery: Wushan – Badong. *Geomorphology*, 84(1/2): 126 – 144. https://doi.org/10.1016/j.geomorph.2006.07.020

Furuki, H., Chigira, M., 2019. Structural Features and the Evolutionary Mechanisms of the Basal Shear Zone of a Rockslide. *Engineering Geology*, 260: 105214. https://doi. org/10.1016/j.enggeo.2019.105214

Gong, W. P., Juang, C. H., Wasowski, J., 2021. Geohazards and Human Settlements: Lessons Learned from Multiple Relocation Events in Badong, China—Engineering Geologist's Perspective. *Engineering Geology*, 285: 106051. https://doi.org/10.1016/j.enggeo.2021.106051

Guthrie, R. H., Friele, P., Allstadt, K., et al., 2012. The 6 August 2010 Mount Meager Rock Slide-Debris Flow, Coast Mountains, British Columbia: Characteristics, Dynamics, and Implications for Hazard and Risk Assessment. *Natural Hazards and Earth System Sciences*, 12(5): 1277 – 1294. https://doi.org/10.5194/nhess-12-1277-2012

Hiraishi, T., Okura, S., 2017. Experimental Study on Effect of Wave Set-up in Storm Surge. *Procedia IUTAM*, 25: 52–59. https://doi.org/10.1016/j.piutam.2017.09.008

Hu, X. D., Zhang, L., Hu, K. H., et al., 2022. Modelling the Evolution of Propagation and Runout from a Gravel-Silty Clay Landslide to a Debris Flow in Shaziba, Southwestern Hubei Province, China. *Landslides*, 19(9): 2199 – 2212. https://doi.org/10.1007/s10346-022-01897-5

Imaizumi, F., Masui, T., Yokota, Y., et al., 2019. Initiation and Runout Characteristics of Debris Flow Surges in Ohya Landslide Scar, Japan. *Geomorphology*, 339: 58 – 69. https://doi.org/10.1016/j.geomorph.2019.04.026

Isbell, J. L., Rubén Cúneo, N., 1996. Depositional Framework of Permian Coal-Bearing Strata, Southern Victoria Land, Antarctica. *Palaeogeography, Palaeoclimatology, Palaeoecology*, 125(1/2/3/4): 217 – 238. https://doi.org/10.1016/S0031-0182(96)00032-6

Jones, D. B., Siddle, H. J., Reddish, D. J., et al., 1991. Landslides and Undermining: Slope Stability Interaction with Mining Subsidence Behaviour. In: Wittke, W., ed., Proceedings of the 7th International Society of Rock Mechanics (ISRM) Congress. International Society for Rock Mechanics, Aachen

Kang, X., Wang, S., Wu, W., et al., 2022. Residual State Rate Effects of Shear-Zone Soil Regulating Slow-to-Fast Transition of Catastrophic Landslides. *Engineering Geology*, 304: 106692. https://doi.org/10.1016/j.enggeo.2022.106692

Kataoka, M., Mahdavi, E., Funatsu, T., et al., 2017. Estimation of Mode I Fracture Toughness of Rock by Semi-Circular Bend Test under Confining Pressure Condition. *Procedia Engineering*, 191: 886–893. https://doi.org/10.1016/j.proeng.2017.05.258

Kojima, S., Nagata, H., Yamashiroya, S. I., et al., 2015. Large Deep-Seated Landslides Controlled by Geologic Structures: Prehistoric and Modern Examples in a Jurassic Subduction – Accretion Complex on the Kii Peninsula, Central Japan. *Engineering Geology*, 186: 44 – 56. https://doi.org/10.1016/j.enggeo.2014.10.018

Li, Z. X., Wang, D. D., Lv, D. W., et al., 2018. The Geologic Settings of Chinese Coal Deposits. *International Geology Review*, 60(5/6): 548–578. https://doi.org/10.1080/00206814.2017.1324327

Loke, M. H., Barker, R. D., 1995. Least-Squares Deconvolution of Apparent Resistivity Pseudosections. *Geophysics*, 60(6): 1682–1690. https://doi.org/10.1190/1.1443900

Loke, M. H., Barker, R. D., 1996. Rapid Least-Squares Inversion of Apparent Resistivity Pseudosections by a Quasi-Newton Method1. *Geophysical Prospecting*, 44(1): 131–152. https://doi.org/10.1111/j.1365-2478.1996.tb00142.x

Pánek, T., Břežný, M., Kapustová, V., et al., 2019. Large Landslides and Deep-Seated Gravitational Slope Deformations in the Czech Flysch Carpathians: New LiDAR-Based Inventory. *Geomorphology*, 346: 106852. https://doi.org/10.1016/j.geomorph.2019.106852

Pazzi, V., Di Filippo, M., Di Nezza, M., et al., 2018. Integrated Geophysical Survey in a Sinkhole-Prone Area: Microgravity, Electrical Resistivity Tomographies, and Seismic Noise Measurements to Delimit Its Extension. *Engineering Geology*, 243: 282–293. https://doi.org/10.1016/j.enggeo.2018.07.016

Qin, S. Q., Xu, X. W., Hu, P., et al., 2010. Brittle Failure Mechanism of Multiple Locked Patches in a Seismogenic Fault System and Exploration on a New Way for Earthquake Prediction. *Chinese Journal of Geophysics*, 53(4): 1001–1014. https://doi.org/10.3969/j.issn.0001-5733.2010.04.025 (in Chinese with English Abstract)

Riesgo Fernández, P., Rodríguez Granda, G., Krzemień, A., et al., 2020. Subsidence Versus Natural Landslides when Dealing with Property Damage Liabilities in Underground Coal Mines. *International Journal of Rock Mechanics and Mining Sciences*, 126: 104175. https://doi.org/10.1016/j.ijrmms.2019.104175

Song, K., Wang, F. W., Zuo, Q. J., et al., 2021. Successful Disaster Management of the July 2020 Shaziba Landslide Triggered by Heavy Rainfall in Mazhe Village, Enshi City, Hubei Province, China. *Landslides*, 18(10): 3503 – 3507. https://doi.org/10.1007/s10346-020-01565-6

Summa, V., Sinisi, R., Paris, E., et al., 2022. Compositional Features of Fine Sediments Involved in the Montescaglioso Landslide (Southern Italy). *Journal of Earth Science*, 33(6): 1513 – 1525. https://doi.org/10.1007/s12583-021-1579-8

Tang, H. M., Jia, H. B., Hu, X. L., et al., 2010. Characteristics of Landslides Induced by the Great Wenchuan Earthquake. *Journal of Earth Science*, 21(1): 104–113. https://doi.org/10.1007/s12583-010-0008-1

Tang, H. M., Zou, Z. X., Xiong, C. R., et al., 2015. An Evolution Model of Large Consequent Bedding Rockslides, with Particular Reference to the Jiweishan Rockslide in Southwest China. *Engineering Geology*, 186: 17–27. https://doi.org/10.1016/j.enggeo.2014.08.021

Tanyaş, H. K., van Westen, C. J., Allstadt, K. E., et al., 2019. Factors Controlling Landslide Frequency-Area Distributions. *Earth Surface Processes and Landforms*, 44(4): 900 – 917. https://doi.org/10.1002/esp.4543

Vassallo, R., Grimaldi, G. M., Di Maio, C., 2015. Pore Water Pressures Induced by Historical Rain Series in a Clayey Landslide: 3D Modeling. *Landslides*, 12(4): 731–744. https://doi.org/10.1007/s10346-014-0508-7

von Ruette, J., Lehmann, P., Or, D., 2016. Linking Rainfall-Induced Landslides with Predictions of Debris Flow Runout Distances. *Landslides*, 13(5): 1097 – 1107. https://doi.org/10.1007/s10346-015-0621-2

Wakizaka, Y., 2013. Characteristics of Crushed Rocks Observed in Drilled Cores in Landslide Bodies Located in Accretionary Complexes. *Tectonophysics*, 605: 114–132. https://doi.org/10.1016/j.tecto.2013.07.018

Wartman, J., Montgomery, D. R., Anderson, S. A., et al., 2016. The 22 March 2014 Oso Landslide, Washington, USA. *Geomorphology*, 253: 275–288. https://doi.org/10.1016/j.geomorph.2015.10.022

Wasowski, J., Pisano, L., 2020. Long-Term InSAR, Borehole Inclinometer, and Rainfall Records Provide Insight into the Mechanism and Activity Patterns of an Extremely Slow Urbanized Landslide. *Landslides*, 17(2): 445–457. https://doi.org/10.1007/s10346-019-01276-7

Wu, D. X., Zhou, J. G., Ren, J. F., et al., 2023. Reconstruction of Depositional Environment and Source-Reservoir Configuration Relationship of Ordovician Majiagou Formation in Ordos Basin. *Earth Science*, 48(2): 553–567 (in Chinese with English Abstract)

Xu, G. L., Li, W. N., Yu, Z., et al., 2015. The 2 September 2014 Shanshucao Landslide, Three Gorges Reservoir, China. *Landslides*, 12(6): 1169 – 1178. https://doi. org/10.1007/s10346-015-0652-8

Xu, Q., Dong, X. J., Deng, M. L., et al., 2010. The Ermanshan Rock Slide-Debris Flow of Junly 27, 2010 in Hanyuan, Sichuan: Characteristics and Failure Mechanism. *Journal of Engineering Geology*, 18(5): 609 – 622. https://doi. org/10.3969/j. issn. 1004-9665.2010.05.003 (in Chinese with English Abstract)

Xue, C. H., Chen, K. J., Tang, H., et al., 2022. Heavy Rainfall Drives Slow-Moving Landslide in Mazhe Village, Enshi to a Catastrophic Collapse on 21 July 2020. *Landslides*, 19(1): 177–186. https://doi.org/10.1007/s10346-021-01782-7

Yang, D. D., Qiu, H. J., Ma, S. Y., et al., 2022. Slow Surface Subsidence and Its Impact on Shallow Loess Landslides in a Coal Mining Area. *Catena*, 209: 105830. https://doi. org/10.1016/j.catena.2021.105830

Yang, Q. G., Yao, X. M., Shen, S. H., et al., 2020. Risk Disposal of Barrier Lake Based on Routine and Emergency Coordinated Management Theory: Case of Tunbao Barrier Lake on Qingjiang River in 2020. *Yangtze River*, 51(12): 25–30. https://doi. org/10.16232/j. cnki. 1001-4179.2020.12.005 (in Chinese with English Abstract)

Yin, Q. F., Tao, P. F., Xia, Y. M., 2020. Active Faults and Bedrock Detection with Super-High-Density Electrical Resistivity Imaging. *Bulletin of Engineering Geology and the Environment*, 79(10): 5049–5060. https://doi.org/10.1007/s10064-020-01867-y

Yoshida, H., Nagatomo, A., Oshima, A., et al., 2014. Geological Characterisation of the Active Atera Fault in Central Japan: Implications for Defining Fault Exclusion Criteria in Crystalline Rocks around Radioactive Waste Repositories. *Engineering Geology*, 177: 93–103. https://doi. org/10.1016/j. enggeo.2014.05.008

Yu, H. B., Li, C. D., Zhou, J. Q., et al., 2022. A Large-Scale Obliquely Inclined Bedding Rockslide Triggered by Heavy Rainstorm on the 8th of July 2020 in Shiban Village, Guizhou, China. *Landslides*, 19(5): 1119 – 1130. https://doi. org/10.1007/s10346-022-01850-6

Zangmo, G. T., Kagou, A. D., Nkouathio, D. G., et al., 2009. Typology of Natural Hazards and Assessment of Associated Risks in the Mount Bambouto Caldera (Cameroon Line, West Cameroon). *Acta Geologica Sinica*: *English Edition*, 83(5): 1008–1016. https://doi.org/10.1111/j.1755-6724.2009.00130.x

Zhang, S. J., Zhao, D. J., Shen, S. W., 2020. Failure Mechanism of Gently Inclined Bedding Slope under Hydraulic Driving: The Case of the Jiangyuan Landslide along Heda Highway. *Journal of Computational Methods in Sciences and Engineering*, 20(2): 383–397. https://doi.org/10.3233/jcm-193748

Zhou, S. Y., Gao, L., Zhang, L. M., 2019. Predicting Debris-Flow Clusters under Extreme Rainstorms: A Case Study on Hong Kong Island. *Bulletin of Engineering Geology and the Environment*, 78(8): 5775–5794. https://doi.org/10.1007/s10064-019-01504-3

Zhou, Z., Zhang, J. M., Ning, F. L., et al., 2020. Large-Scale Test Model of the Progressive Deformation and Failure of Cracked Soil Slopes. *Journal of Earth Science*, 31(6): 1097–1108. https://doi.org/10.1007/s12583-020-1342-6